ADF 300 929

(12)

DTIC FILE COPY

AD

AD-A184 247

TECHNICAL REPORT BRL-TR-2812

NITROGUANIDINE MORPHOLOGY IN EXTRUDED GUN PROPELLANT

ROBERT J. LIEB

JUNE 1987

APPROVED FOR PUBLIC RELEASE; DISTRIBUTION UNLIMITED.

US ARMY BALLISTIC RESEARCH LABORATORY
ABERDEEN PROVING GROUND, MARYLAND

87 9 9 291

Unclassified
SECURITY CLASSIFICATION OF THIS PAGE

A184247

REPORT DOCUMENTATION PAGE

Form Approved
OMB No 0704-0188
Exp. Date Jun 30, 1986

1a. REPORT SECURITY CLASSIFICATION Unclassified	1b. RESTRICTIVE MARKINGS
2a. SECURITY CLASSIFICATION AUTHORITY	3. DISTRIBUTION/AVAILABILITY OF REPORT
2b. DECLASSIFICATION/DOWNGRADING SCHEDULE	
4. PERFORMING ORGANIZATION REPORT NUMBER(S)	5. MONITORING ORGANIZATION REPORT NUMBER(S)
6a. NAME OF PERFORMING ORGANIZATION US Army Ballistic Research Lab 6b. OFFICE SYMBOL (If applicable) SLCBR-IB-P	7a. NAME OF MONITORING ORGANIZATION
6c. ADDRESS (City, State, and ZIP Code) Aberdeen Proving Ground, MD 21005066	7b. ADDRESS (City, State, and ZIP Code)
8a. NAME OF FUNDING/SPONSORING ORGANIZATION 8b. OFFICE SYMBOL (If applicable)	9. PROCUREMENT INSTRUMENT IDENTIFICATION NUMBER
8c. ADDRESS (City, State, and ZIP Code)	10. SOURCE OF FUNDING NUMBERS PROGRAM ELEMENT NO. | PROJECT NO. | TASK NO. | WORK UNIT ACCESSION NO

11. TITLE (Include Security Classification)
NITROGUANIDINE MORPHOLOGY IN EXTRUDED GUN PROPELLANT

12. PERSONAL AUTHOR(S)
Lieb Robert James

13a. TYPE OF REPORT	13b. TIME COVERED	14. DATE OF REPORT (Year, Month, Day)	15. PAGE COUNT
Final	FROM 850101 TO 860101		

16. SUPPLEMENTARY NOTATION
Initial results published in the proceedings of the 22nd JANNAF Combustion Meeting, CPIA Publication 432.

17. COSATI CODES			18. SUBJECT TERMS (Continue on reverse if necessary and identify by block number)
FIELD	GROUP	SUB-GROUP	Gun Propellant, Nitroguanidine, Morphology, Extrusion, Burning Rate, Mechanical Properties

19. ABSTRACT (Continue on reverse if necessary and identify by block number)

During a study of M31A1 and M30 experimental propellants, ring patterns were discovered between the perforation holes in the outer web on the ends of grain specimens which had been prepared for impact mechanical properties measurements. No known source had ever reported this type structure. A study using both optical and scanning electron microscopy was undertaken to discover the morphological structure responsible for the rings. Results indicate that this morphology is common in extruded propellant containing nitroguanidine (NQ) crystals. The ring structure results from bands of NQ crystals that are folded in a zigzag pattern. These patterns are observed in regions that would be expected to have high flow during the extrusion process, and are caused by pin plate feed holes. NQ crystal alignment in the direction of extrusion was found in regions were large velocity gradients exist during extrusion. Dynamic mechanical properties measurements indicated that these morphological structures have little affect on the mechanical response of the propellants. Closed bomb testing, however, indicated that the burning rate of M30 was affected by the difference between the aligned and folded NQ morphology.

20. DISTRIBUTION/AVAILABILITY OF ABSTRACT X UNCLASSIFIED/UNLIMITED ☐ SAME AS RPT ☐ DTIC USERS	21. ABSTRACT SECURITY CLASSIFICATION UNCLASSIFIED
22a. NAME OF RESPONSIBLE INDIVIDUAL ROBERT J. LIEB	22b. TELEPHONE (Include Area Code) (301)278-6195 22c. OFFICE SYMBOL SLCBR-IB-P

DD FORM 1473, 84 MAR
83 APR edition may be used until exhausted
All other editions are obsolete

SECURITY CLASSIFICATION OF THIS PAGE
Unclassified

TABLE OF CONTENTS

		Page
	LIST OF ILLUSTRATIONS	5
I.	INTRODUCTION	7
II.	EXPERIMENTAL METHOD AND RESULTS	7
	A. Propellant Grain Structure	7
	B. Solid Strand M30 Propellant Structure	15
	C. Solid Strand M30 Mechanical Properties	20
III.	ANALYSIS AND DISCUSSION	25
	A. Propellant Morphology	25
	B. Effects of Propellant Morphology	27
IV.	CONCLUSIONS	30
V.	ACKNOWLEDGMENT	32
	REFERENCES	33
	DISTRIBUTION LIST	35

LIST OF ILLUSTRATIONS

Figure		Page
1	Optical Photograph of M31A1 Lot 07077 Showing the Ring Structure between the Outer Perforations	9
2	SEM Photograph of M31A1 Showing the Ring Structure	10
3.	Illustration of Type A and Type B Fractures in Propellant Grains	10
4	SEM Photographs of the Type A Cold Fracture Surface of the Grain Shown in Figure 2 Showing the Structure Responsible for the Rings	11 - 13
5	SEM Photographs of M30 Propellant with Type B Fracture	14
6	Schematic Diagram Illustrating the Extrusion Process	16
7	Photographs of M30 Solid Strand Extruded with Pin Plate	17
8	Photographs of M30 Solid Strand Extruded after Remixing and Pin Plate Removed	18
9	M30 Strand Fracture Surface From Strand Shown in Figure 7a	19 - 20
10	M30 Strand Fracture Surface From Strand Shown in Figure 7b	21
11	M30 Strand Fracture Surface From Strand Shown in Figure 8a	22
12	Dynamic Mechanical Analysis Results Showing Modulus vs Temperature for M30. Solid Line is Drop Weight Results of a Reference Lot	23
13	Dynamic Mechanical Analysis Results Showing Temperature and Modulus vs Time for an M30 Strand Showing the Thermal Lag of the Specimen	24
14	Schematic Diagram Illustrating the Extrusion Process and a Possible Method for the Formation of Bands of Folded NQ within the Grain	26
15	Representative Dynamic Mechanical Analysis Results Showing Modulus and Tan Delta vs Temperature for M30	28

LIST OF ILLUSTRATIONS (CONT'D)

Figure		Page
16	Closed Bomb Burning Rate vs Pressure for M30 Showing a Slope Break at about 10 kpsi (69 MPa)	29
17	Pressure at Slope Break vs Loading Density from Closed Bomb Burning Rate Studies	31

I. INTRODUCTION

During sample preparation for mechanical properties testing, ring-like structures were observed on the ends of multiperforated propellant grains. This structure was revealed first in experimental M31A1 gun propellant, produced as part of a nitroguanidine (NQ) particle size study. The structure was found in eight experimental lots and in the reference lot of M31A1. The same patterns were also discovered in the reference and eight experimental lots of M30 propellant, also as part of the NQ study. These rings and the morphology producing them seem to be common to extruded propellant containing NQ.

The morphology of propellants can affect the combustion of these materials in several ways. First, since the mechanical response of the propellant can be greatly influenced by processing and the resulting structure, the morphology and factors controlling the morphology may be very important. For example, propellant mechanical properties and fracture response have been shown to have a large effect on piezometric efficiency[1], safety[2,3], and are suspected to have similar effects on the vulnerability. In fact, all recent, low temperature overpressures in large caliber guns have been attributed to propellant fracture occurring early in the ballistic cycle. Also, more subtle effects are possible, such as changes in burning rate or ignitability due to different morphologies being exposed to the flame as the grain burns. In any case, the structure uncovered here provides an opportunity to expand the understanding of processing variables and their effects on propellant combustion.

II. EXPERIMENTAL METHOD AND RESULTS

A. Propellant Grain Structure

Two propellant formulations, M31A1 and M30, were undergoing fracture response characterization when a ring structure at the grain ends was revealed

---

[1] C. W. Fong and B. K. Moy, "Ballistic Criteria for Propellant Grain Fracture In the GAU-8/A 30MM Gun," Technical Report AFATL-TR-82-21, Air Force Armament Laboratory, Direct Fire Weapons Division, Eglin AFB, Florida, March 1982.

[2] P. Benhaim, J. L. Paulin, B. Zeller, "Investigation on Gun Propellant Break-Up and Its Effect in Interior Ballistics," Proceedings of the 4th International Symposium on Ballistics, Monterey, CA, October 1978.

[3] A. W. Horst, I. W. May, and E. V. Clark "The Missing Link Between Pressure Waves and Breechblows," Ballistic Research Laboratory Report ARBRL-MR-02849, July 1978.

TABLE 1. PROPELLANT COMPOSITION

Component	Percent M31A1	Percent M30
Nitrocellulose	20.00	28.00
(Percent Nitration)	12.65	12.60
Nitroglycerin	19.00	22.50
Nitroguanidine	54.00	47.70
Dibutylphthalate	4.50	-
Ethyl Centralite	-	1.50
2-Nitrodiphenylamine	1.50	-
Potassium Sulfate	1.00	-
Graphite	0.15	0.10
Cryolite	-	0.30
Ethyl Alcohol	0.30	0.30

as a result of the specimen preparation. The gun propellants are triple base, consisting of a nitrocellulose binder, nitroglycerin plasticizer, and nitroguanidine filler. The percent compositions for each propellant are listed in Table 1. During preparation for mechanical properties testing, the grain, which is in the form of a right circular cylinder, must have its ends flat, parallel, and perpendicular to the cylinder axis; this was done by machining the grains with an end mill. When this was done for the M31A1 reference Lot 070077, white ring patterns, shown in Figure 1, appeared. Similar patterns appeared in all other M31A1 specimens. Since this structure had never been observed before, further investigations were conducted to explain the formation and nature of the rings.

The M31A1 specimen shown in Figure 1 was prepared for investigation using a scanning electron microscope (SEM). Figure 2 shows the resulting SEM photograph, and demonstrates the morphological nature of the rings. The long sweeping arcs are the result of machining required to flatten the end surfaces for testing. Higher magnification photos showed that each ring seemed to be a path formed by a series of voids. Since it was difficult to determine if the apparent porosity was intrinsic to the grain or generated by the preparation procedure, this grain was prepared for further investigation by being cold fractured along a line from midweb to midweb, through the middle of the ring structure and middle perforation. Fractures, such as this one, running through the center of opposite ring structures will subsequently be referred to as a Type A Fracture, which is illustrated in Figure 3. Cold fracturing is achieved by slowly cooling the grain in dry ice. A cold razor edge is then placed along a line defining where the crack is to begin, and a hammer strike initiates the crack propagation. The resulting crack exposes new surface that is neither stretched nor torn and, due to the brittle nature of the low temperature fracture, the inner structure of the material is revealed with little disturbance.

This newly exposed surface is shown in Figure 4. Figure 4a shows the entire fractured grain surface that resulted from a Type A crack propagated in the grain shown in Figure 2. The left side best shows bands that arc from the outside surface to the center perforation, at the center of the picture. These bands were found to be characteristic of midweb fractures in grains that

Nc

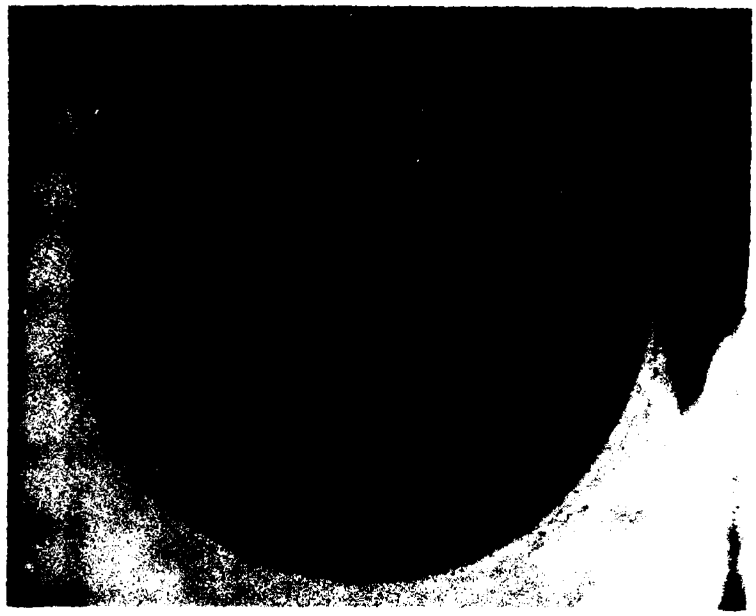

a. The Entire Grain End

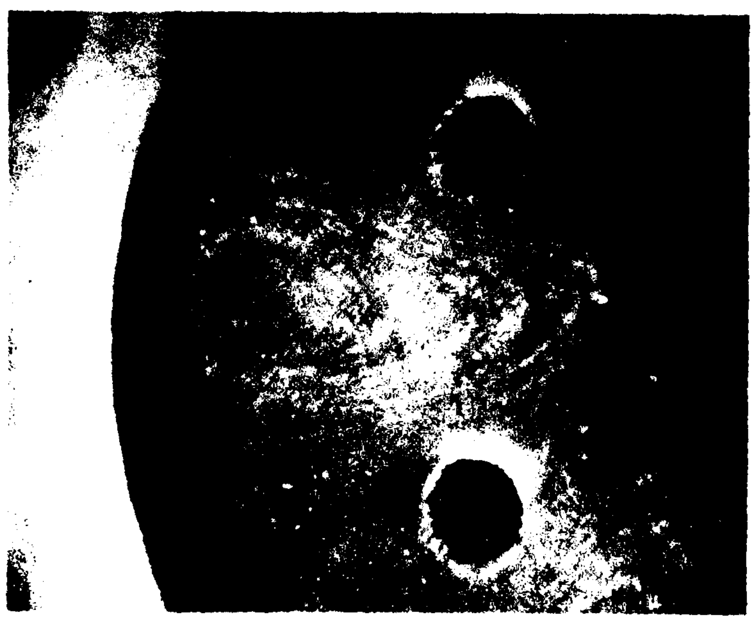

b. Detail of Figure 1a.

Figure 1. Optical Photograph of M31A1 Lot 07077 Showing the Ring Structure between the Outer Perforations

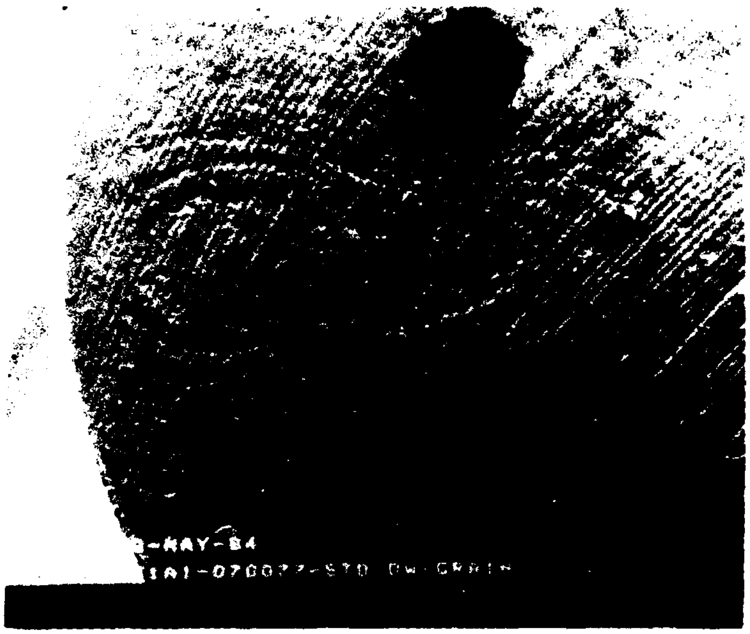

Figure 2. SEM Photograph of M31A1 Showing the Ring Structure

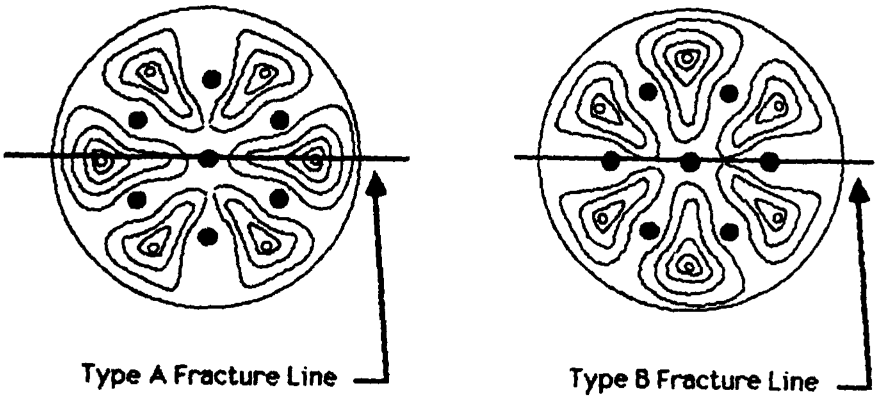

Figure 3. Illustration of Type A and Type B Fractures in Propellant Grains

showed the ring patterns. Figure 4b shows the bands enlarged (Figure 4e illustrates the spatial relationship among photos in Figure 4). The outside of the grain is to the left, and the center perforation runs from top to bottom just off to the right of the photo. Figures 4c shows the center web at a magnification of 100X and reveals the zigzag pattern of the NQ. Near the outside surface all the NQ crystals were strongly aligned in the direction of

a. Entire Fracture Surface

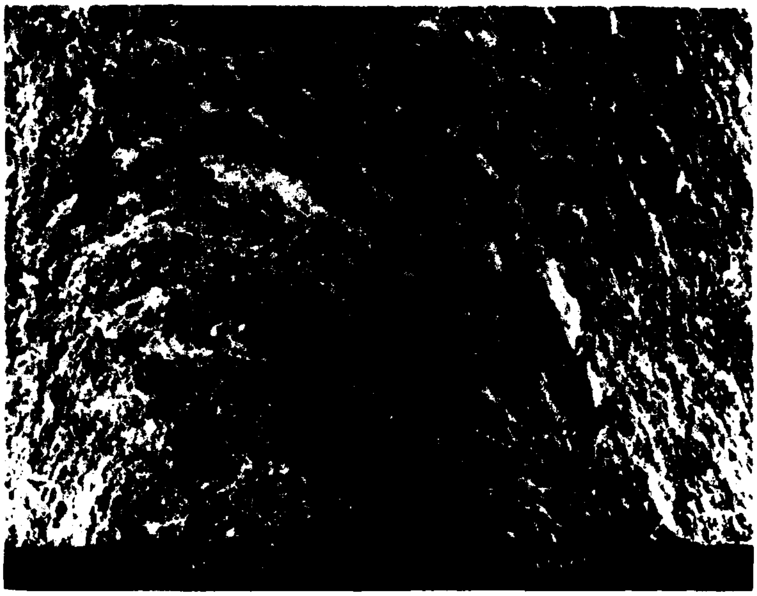

b. Bands of Folded NQ Arcing from Outside Surface to Center Perforation

Figure 4. SEM Photographs of the Type A Cold Fracture Surface of the Grain Shown in Figure 2 Showing the Structure Responsible for the Rings

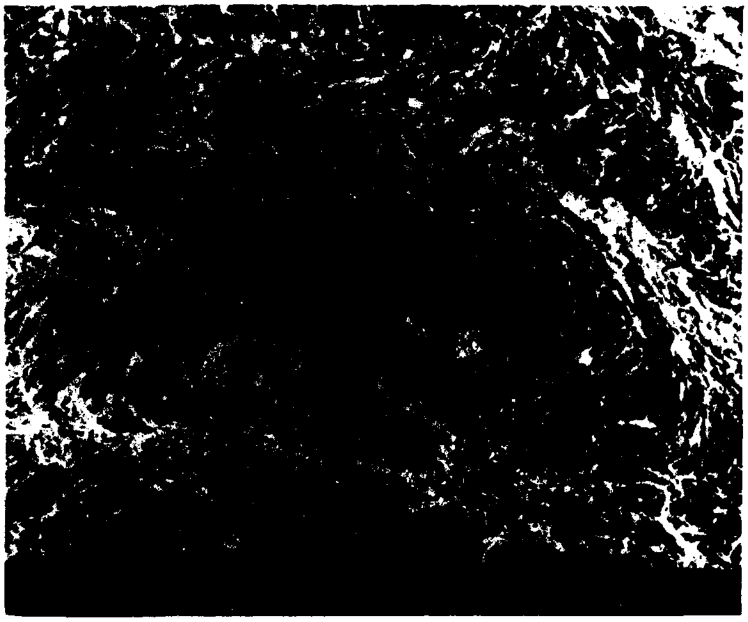

c. Detail of Figure 4b Showing NQ Folding within the Band

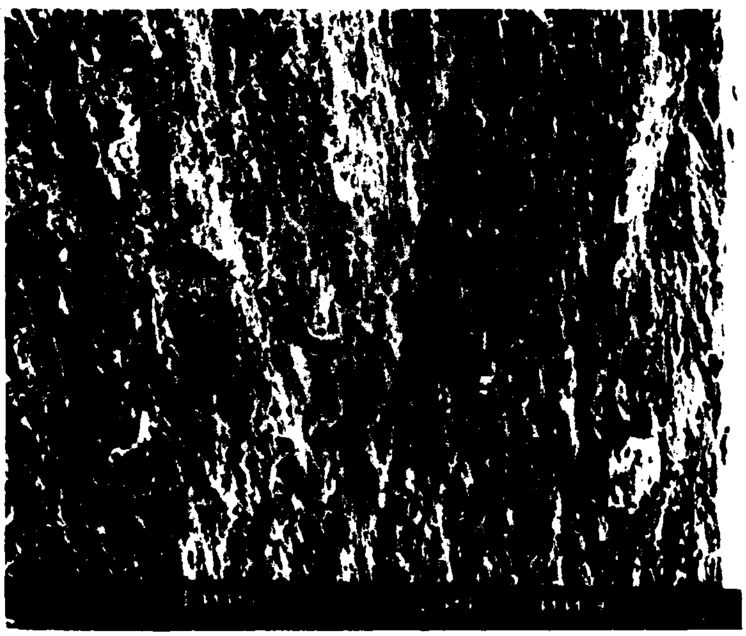

d. Detail of Figure 4a Showing NQ Alignment Near the Center Perforation

Figure 4. SEM Photographs of the Type A Cold Fracture Surface of the Grain Shown in Figure 2 Showing the Structure Responsible for the Rings

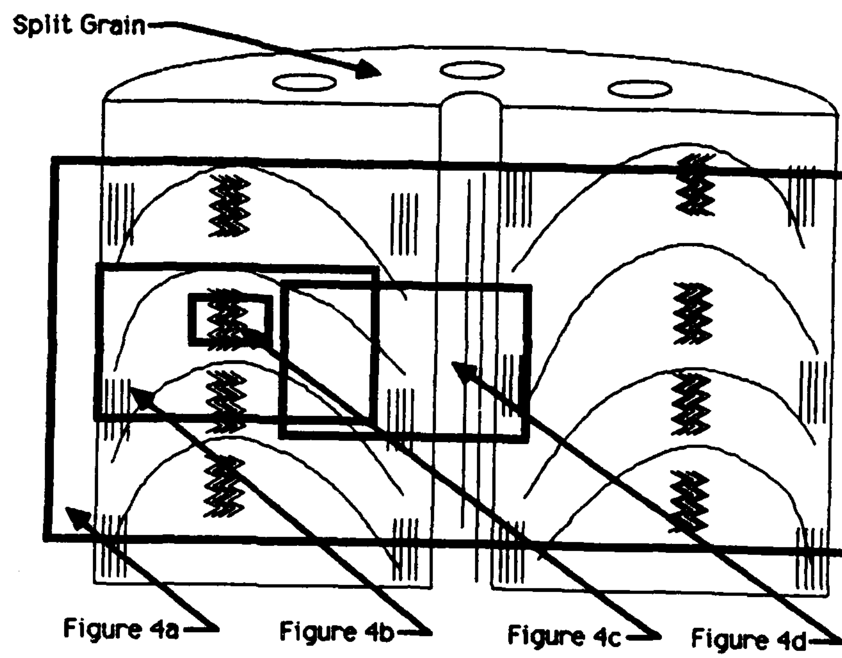

e. Schematic Diagram Showing the Relationship among the Photos in Figure 4 to the Split Grain and Each Other

Figure 4. SEM Photographs of the Type A Cold Fracture Surface of the Grain Shown in Figure 2 Showing the Structure Responsible for the Rings

extrusion and there was no folding. This alignment occurred again to a lesser degree, as Figure 4d shows, near the center perforation, which is running from top to bottom on the right. In this photo the NQ is aligned parallel to the direction of extrusion, and none of the midweb zigzag pattern is present.

The NQ morphology description above is in sharp contrast to the morphology thought to exist based on previous observations. Ordinarily the orientation for grain fracture had been along a row of three perforations. This was done to produce a crack that had clean, flat surfaces that were easily investigated. Fractures running between adjacent ring structures will subsequently be called a Type B Fracture, which is illustrated for a propellant grain in Figure 3. Figure 5 shows what is seen in such a fracture. The NQ was everywhere aligned in the direction of extrusion. There were no bands, and no zigzag patterns. This type of alignment was observed for all Type B fractures in the propellant grains that showed ring patterns. The conclusion drawn from observations such as these was that the NQ aligns in the direction of extrusion, and it was assumed that the alignment continued into the web. From Figure 1 it can be seen that along any row containing the center perforation no ring pattern is intersected and the underlying morphology that produces the rings is therefore not observed.

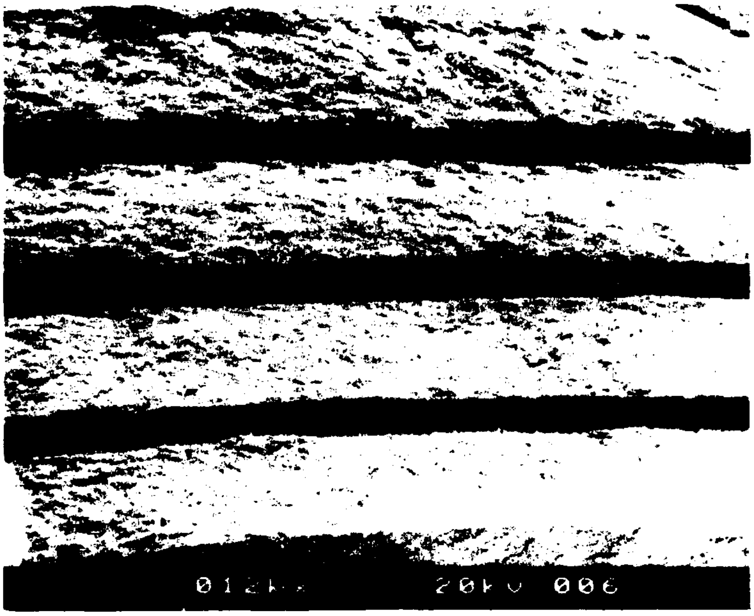

a. Fracture Surface Showing the Web Region between Three Perforations

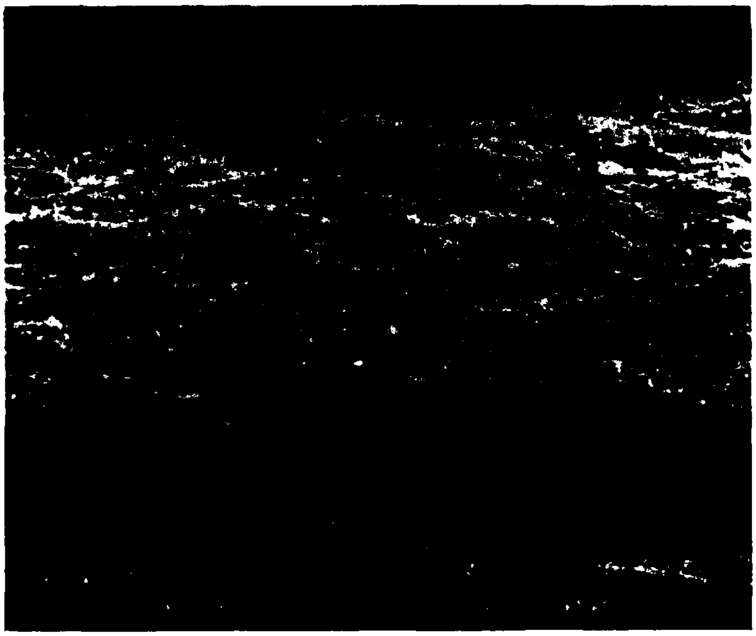

b. Detail of Figure 5a Showing NQ Alignment (30X)

Figure 5. SEM Photographs of M30 Propellant with Type B Fracture

Observations were made on one reference and eight experimental lots of each propellant type with similar results. In every grain investigated there were bands of folded (zigzag) NQ in the midweb regions between the outside perforations. Near any extrusion surface (outside or perforation) and in the regions between three collinear perforations, the NQ crystals were aligned in the direction of extrusion. The degree of alignment and folding varied with web size, NQ particle size, propellant type, and processing differences, but the overall features outlined above remained the same. It should be noted that the bright orange stabilizer in the M31A1 propellant caused these rings to be easily seen with the unaided eye. The ring patterns in the M30 were much more difficult to see and were only successfully photographed using light transmitted through the sample. This may explain why these features have gone unnoticed.

B. Solid Strand M30 Propellant Structure

In another investigation concerned with the effects of normal vs specially ground NQ in M30, solid strands containing either normal or ball-milled NQ were extruded. The extrusion press, as it is assembled for seven perforated propellant strand production, is illustrated in Figure 6. It is the usual practice, even when extruding solid propellant strands, that the pin plate be kept within the die. So, in this solid strand extrusion, the pin plate, which normally contains feed holes and pins was used in the die with the pins removed. Because of flow problems during the extrusion of these lots, remixes (resolvation of the nitrocellulose binder) were made. To reduce the probability of flow problems reoccurring during the second extrusion, the pin plate was removed from die for both the normal and ground NQ remixes. What resulted from the procedure outlined above was four different propellant strands. Normal NQ and ground NQ strands produced with the pin plate in position, and normal NQ and ground NQ strands that were produced without the pin plate. In Figure 7a the cross section of the normal-NQ M30 propellant strand from the first extrusion shows ring patterns similar to those observed in the perforated grains. In Figure 7b, the ground NQ propellant strand shows no ring structure, but only darkened regions which correspond to the usual ring locations. The corresponding remixed lots, produced without the pin plate, are shown in Figure 8, and show no structure. In the photographs in Figures 7 and 8, the image was formed from light traveling through the sample, since the patterns could not be recorded using reflected light.

The SEM investigation of the solid strand specimens that showed ring-like structures revealed that the same morphology responsible for the rings in the perforated grains also produced the structure in the solid strands. Figure 9a shows a section of M30 strand from the same lot shown in Figure 7a. The section was cold fractured with a Type A Fracture revealing bands which are most prominent in the upper left-hand part of the surface. As in the perforated grains, strong NQ alignment occurred near the outside surface (at the top) and in the center region of the strand. NQ folding occurred within the bands and is shown in Figure 9b. The cold fracture surface resulting from a Type B Fracture is shown in Figure 9c. Here, there are no bands and the NQ was aligned in the direction of extrusion across the entire diameter. Two specimens from the ground NQ lot (shown in Figure 7b) were cold fractured in the same way. Figure 10a shows the bands on the surface of the Type A

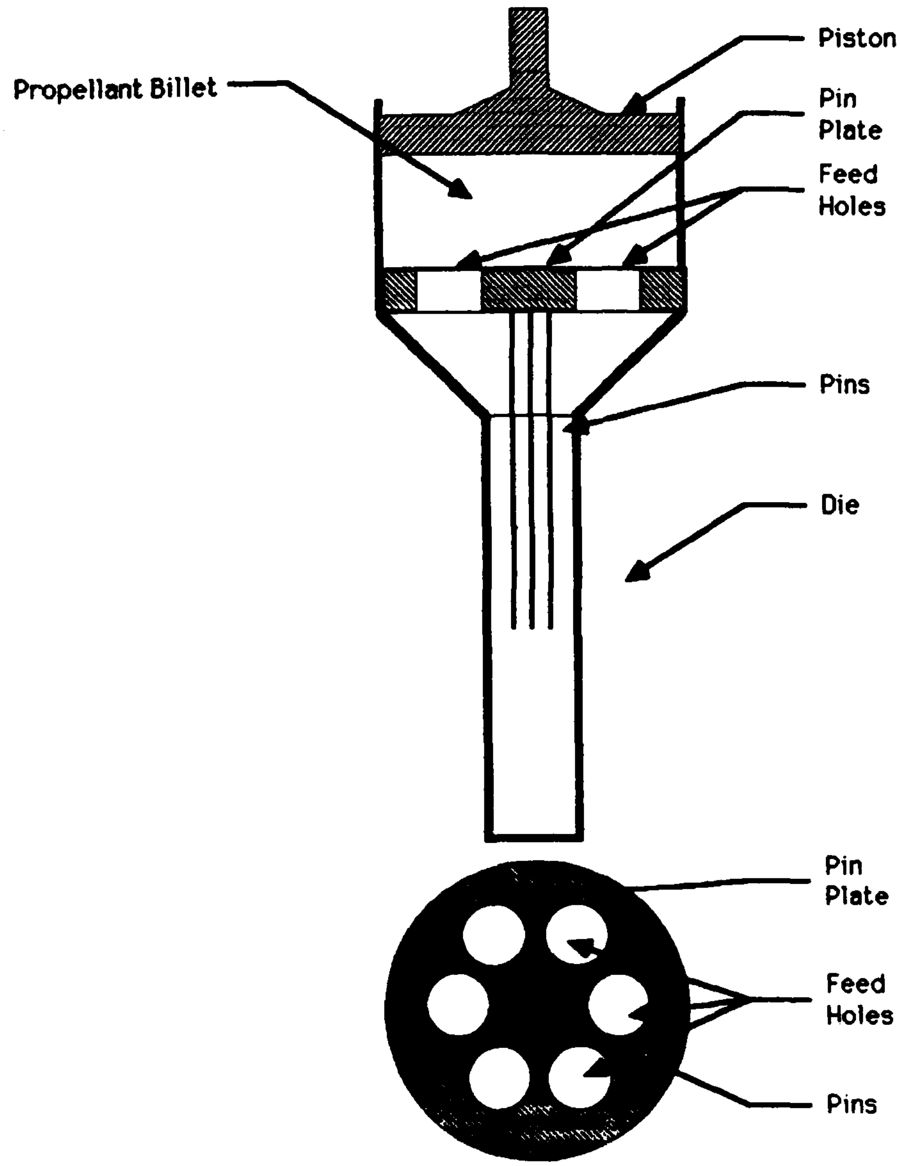

Figure 6. Schematic Diagram Illustrating the Extrusion Process

Fracture on the left (the direction of extrusion in these photos is down). The NQ folding within the bands is much less distinct, due to the shorter NQ crystals. However, parallel alignment is observed in the central and outside surface regions as found for other Type A Fractures. The fracture surface in Figure 10b is Type B and shows uniform alignment of the NQ across the specimen diameter. One significant difference between these and the perforated lots is the shape of the rings. In the propellant grains the rings are altered by the presence of perforation pins. NQ alignment due to drag seems to cause the rings to curve away from the perforations, which results in a squeezed appearance of the rings as compared to the rings formed in the unperforated strand.

a. M30 with Normal NQ

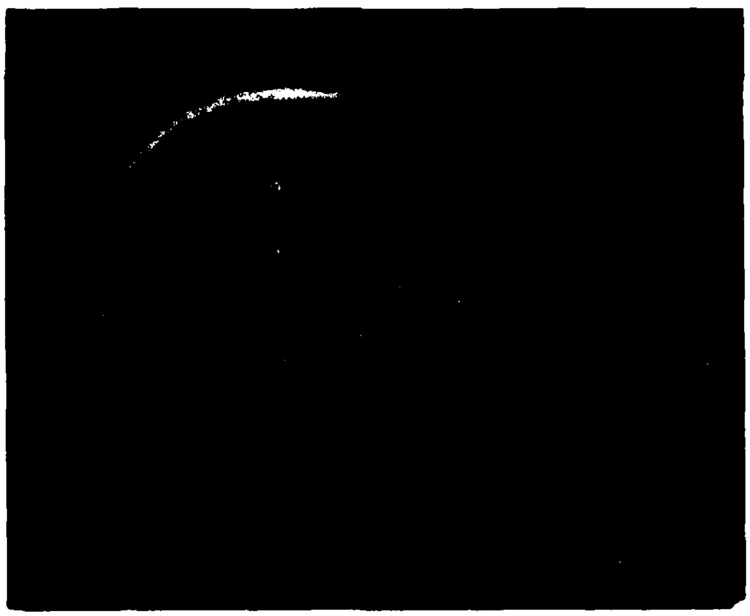

b. M30 with Ground NQ

Figure 7. Photographs of M30 Solid Strand Extruded with Pin Plate

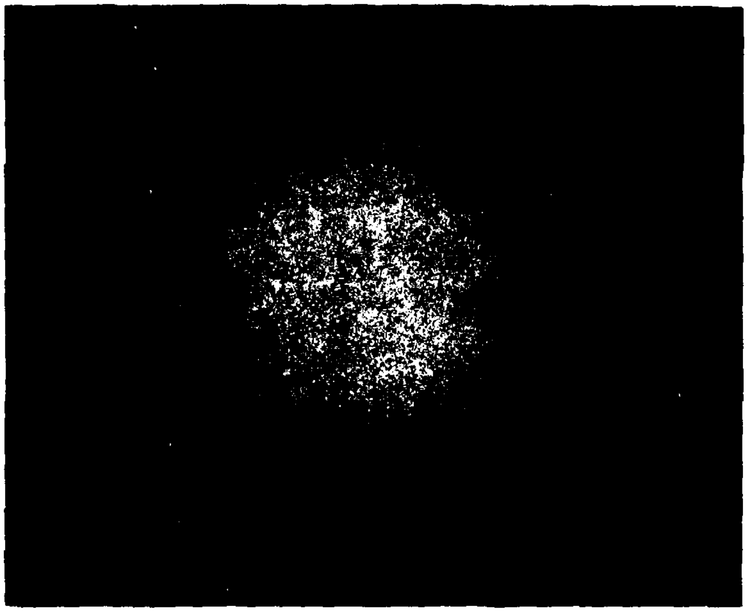

a. M30 with Normal NQ

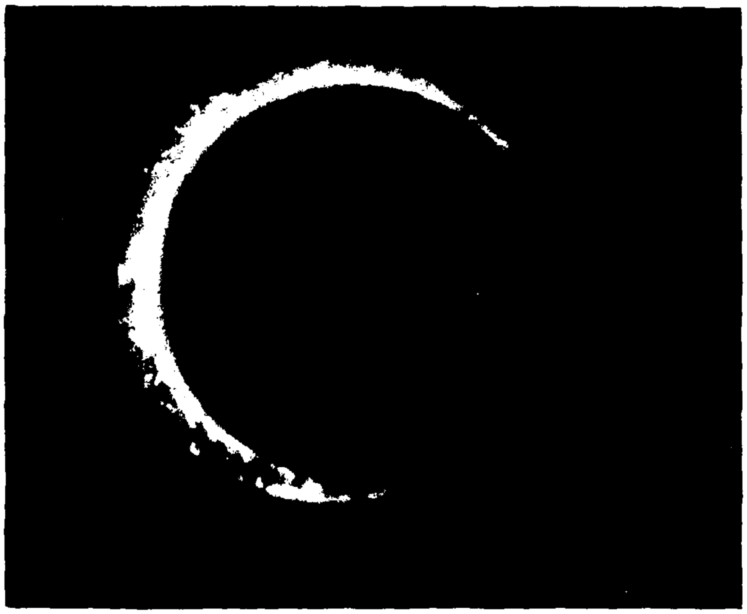

b. M30 with Ground NQ

Figure 8. Photographs of M30 Solid Strand Extruded after Remixing and Pin Plate Removed

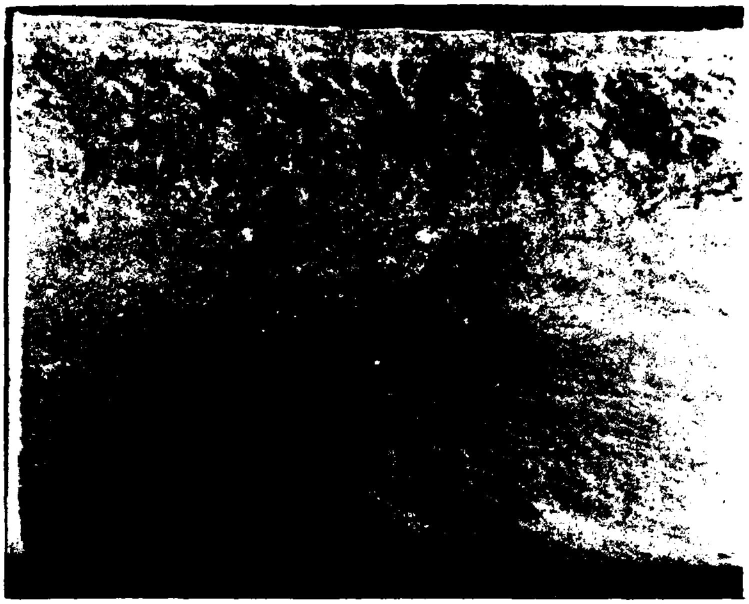

a. Type A Fracture Showing Bands

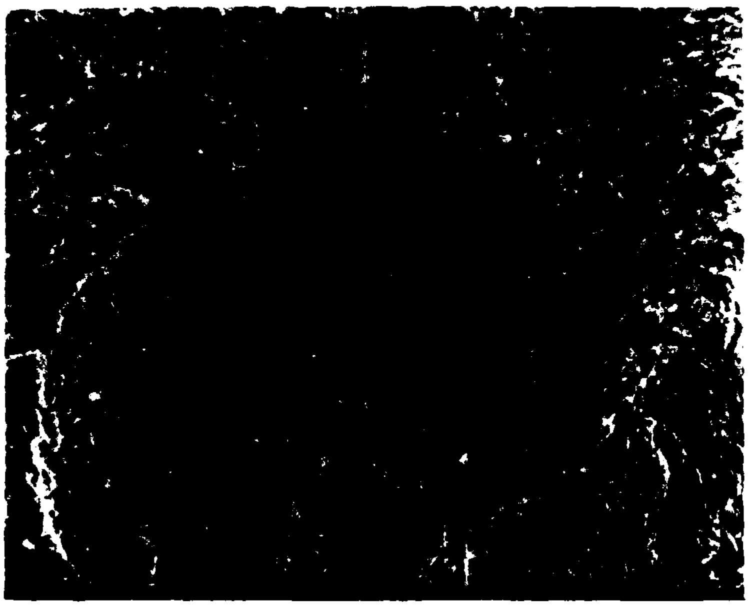

b. Detail of 9a Showing NQ Folding from Midband Region

Figure 9. M30 Strand Fracture Surface From Strand Shown in Figure 7a

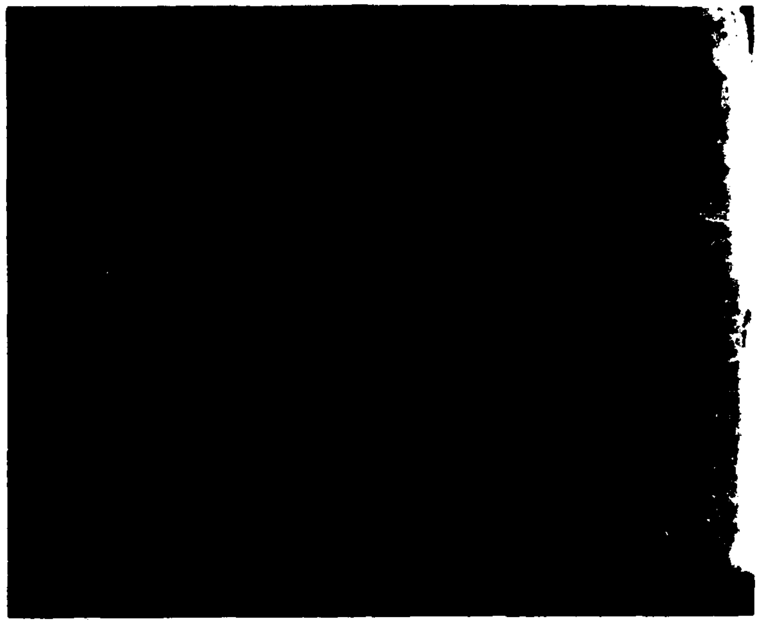

c. Type B Fracture with No Bands

Figure 9. M30 Strand Fracture Surface From Strand Shown in Figure 7a

The remixed lots which showed no structure were cold fractured and also examined with the SEM. The normal NQ lot showed strong NQ alignment across the entire diameter. To ensure that this NQ alignment observation was not due to an inadvertent Type B Fracture, the half grain was again split in half. If a Type B Fracture was made and if the folded NQ structu[illegible]owed the six-fold symmetry found in other specimens, the new fractu[illegible]ace should be Type A and reveal the folded NQ structure. The secon[illegible]acture surface appeared no different than the initial surface, which sugge[illegible]that the lack of observed rings indicates a lack of bands of folded NQ. Figure . shows the center section of the initial surface of the remixed strand, and reveals a mild folding of the NQ crystals. The "tightness" of the folding is much less, i.e. the distance between repeating forms is longer, and the folding amplitude is much smaller, but the folding found in the center of this propellant strand seems the same in nature as the folding appearing in the centers of the six ring structures, although on quite a different scale. The remixed ground propellant lot showed a reduced NQ alignment in the direction of extrusion due to the shorter NQ length, and no NQ folding near the center of the grain.

C. Solid Strand M30 Mechanical Properties

Mechanical properties tests were performed on these strands for comparison between the propellant with and without the ring structure, and for comparison with the mechanical properties measurements made previously on perforated lots. Since a very limited supply of solid strand propellant was available, the tests were performed nondestructively with the DuPont 982

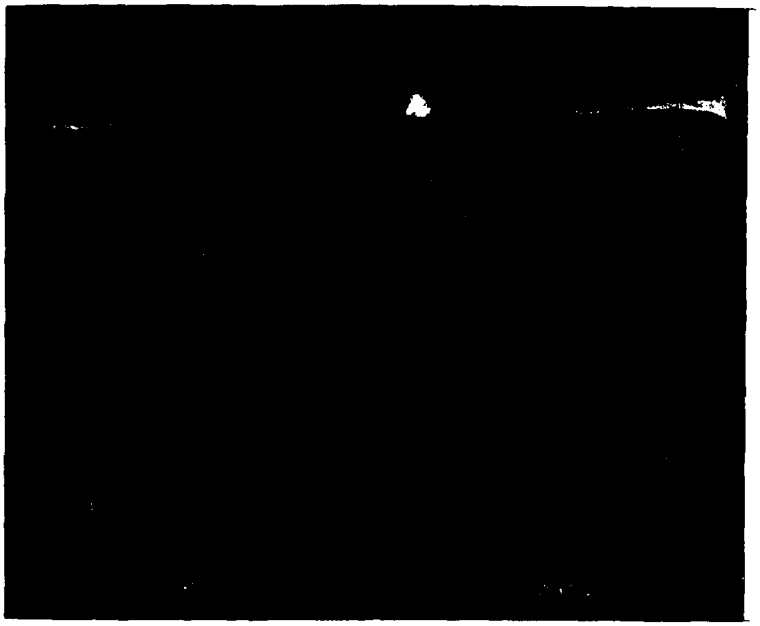

a. Type A Fracture Showing Bands

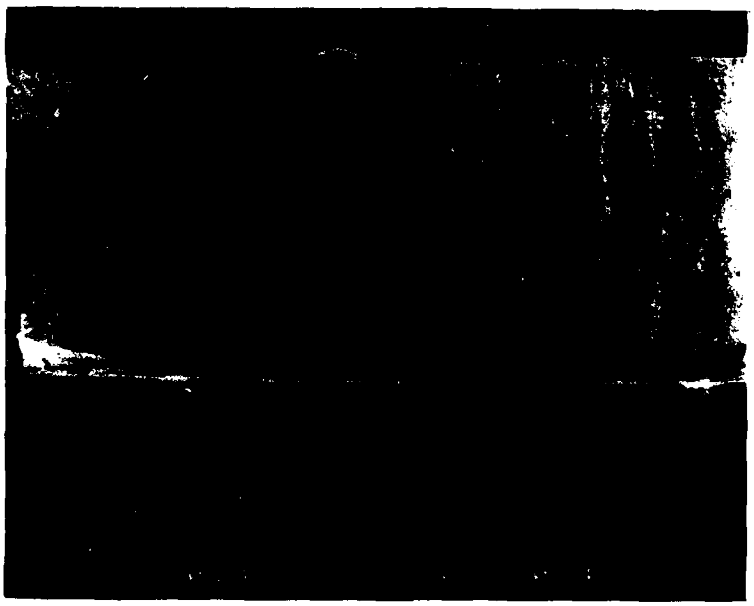

b. Type B Fracture with no Bands

Figure 10. M30 Strand Fracture Surface From Strand Shown in Figure 7b

a. Cold Fracture Surface with No Band Structure

b. Detail of Figure 11a from Midstrand Showing Very Mild NQ Folding

Figure 11. M30 Strand Fracture Surface From Strand Shown in Figure 8a

Dynamic Mechanical Analyzer (DMA). Much literature is available on this tester[4]. Briefly, the mechanical properties are calculated from the measurement of the resonance frequency of the sample/instrument system and the damping signal required to maintain constant oscillation amplitude.

Measurements were made from -60 to 100°C, and the resulting modulus values are presented in Figure 12. The plot indicates that no outstanding differences exists among the propellant curves, and that the DMA results agree fairly well with the high rate measurements made with the Drop Weight

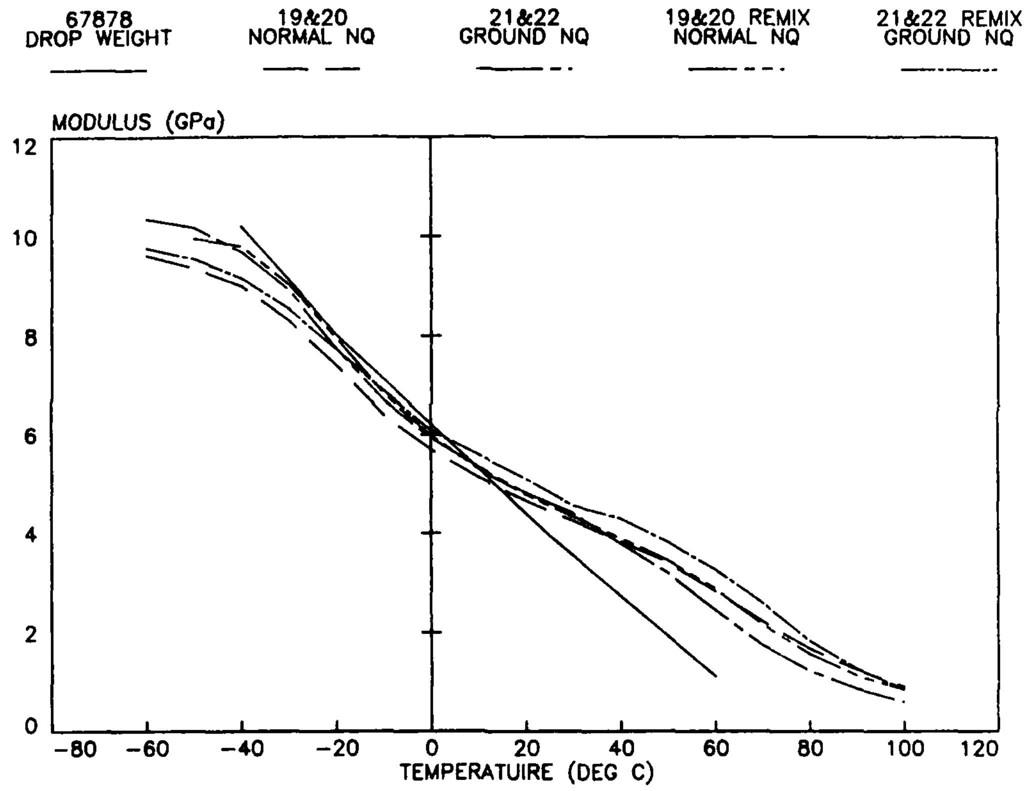

Figure 12. Dynamic Mechanical Analysis Results Showing Modulus vs Temperature for M30. Solid Line is Drop Weight Results of a Reference Lot

[4] R. L. Hassel, "Evaluating Polymers by Dynamic Mechanical Analysis," Plastics Engineering, Vol. 33, No. 10, October 1977.

Mechanical Properties Tester (DWMPT)[5]. The DWMPT results were gathered at ambient pressures and at a rate of about 225 s^{-1}. The difference in modulus between the DMA and DWMPT above room temperature is attributed to thermal lag of the specimen, due to the relatively high heating rate of $5^{o}C/min$ used for all DMA runs.

Figure 13 shows the results of an isothermal run which was used to indicate the degree of thermal lag at higher temperatures. In this run the

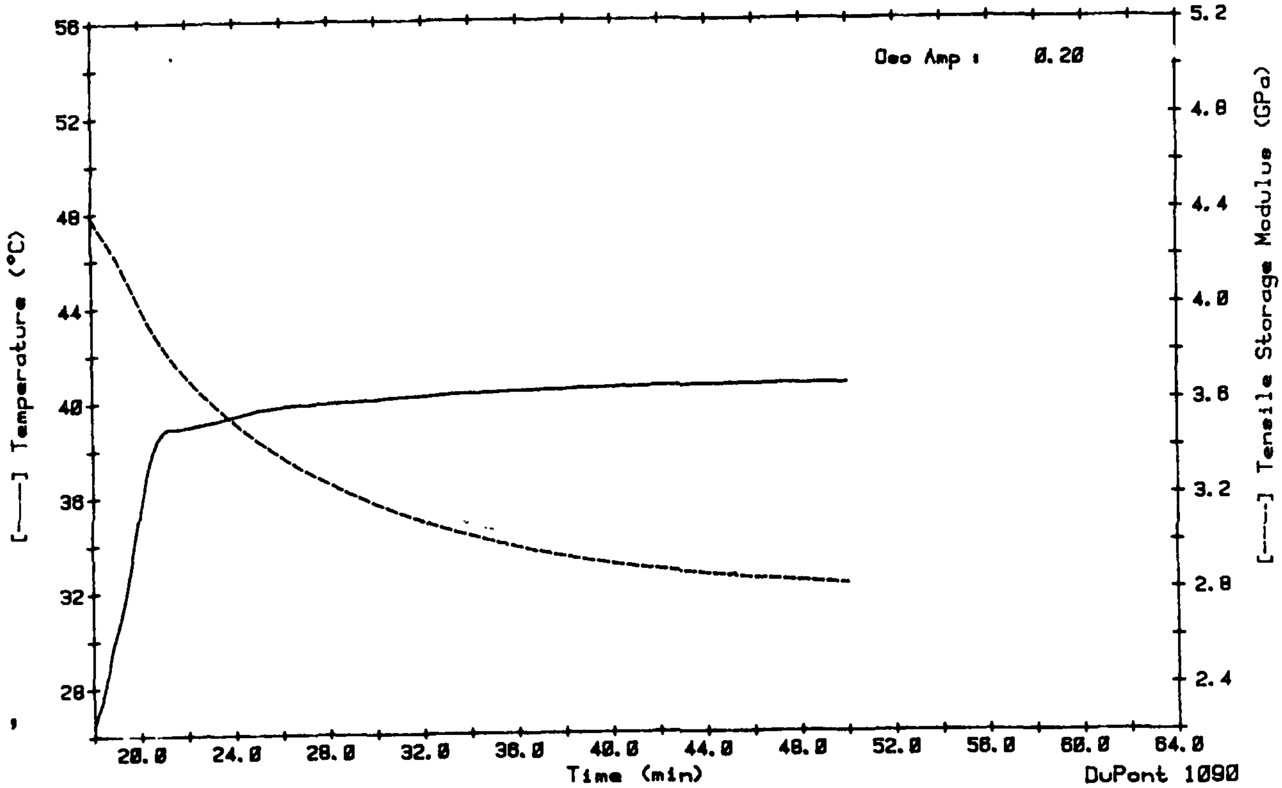

Figure 13. Dynamic Mechanical Analysis Results Showing Temperature and Modulus vs Time for an M30 Strand Showing the Thermal Lag of the Specimen

---

[5] R. J. Lieb, and J. J. Rocchio, "Standardization of a Drop Weight Mechanical Properties Tester for Gun Propellants," Technical Report ARBRL-TR-02516, USA ARRADCOM Ballistic Research Laboratory, Aberdeen Proving Ground, Maryland, July 1983.

temperature was increased from -60°C at 5°C/min to 40°C and then held at 40°C for 30 minutes while the mechanical properties were monitored. As the temperature was held near constant the modulus continued to decrease for the entire 30 minute period. Although the modulus is approaching a constant value, a significant thermal gradient is indicated. Measurements at room temperature taken while the sample was known to be in thermal equilibrium gave modulus values of about 3.5 GPa, much closer to and lower than the DWMPT values, which puts the effective thermal lag for these specimens at about 20°C. The strands of M30 tested all had about the same diameter, so thermal lag should be nearly the same for each specimen. If differences in mechanical properties existed among the strands, the thermal lag problem should not hinder that measurement.

III. ANALYSIS AND DISCUSSION

A. Propellant Morphology

The ring patterns on the grain ends are the result of a combination of the NQ folding, shown in Figure 4b and 4c, the curved bands stretching from the outside surface to the inner perforation, as shown in Figure 4a , and the preferential cutting caused by the surface preparation tool. A surface cut perpendicular to the axis of the grain would expose parts of several bands. Since each band has one or more changes in the orientation of the NQ, a ring pattern appears corresponding to that changing NQ orientation and the different cutting resistance offered by the microcrystal orientation. Other surface preparation techniques (fine grit sandpaper, diamond saw) produce less distinct ring patterns on specimens from the same lots. This indicates that the surface preparation plays a role in the appearance of the grain ends. The actual shape of the rings is understood realizing that the bands are actually a two dimensional intersections of a three dimensional dome structure that contains these folded NQ regions. A ring forms (in the case of the end mill preparation) as an outline of the region containing similar cutting conditions, By examining Figure 1 and the corresponding orthogonal view in Figure 4a, it can be seen that this relationship is demonstrated.

Examination of various experimental lots which contained different combinations of web and NQ particle sizes indicated that less regular patterns seem to result from larger webs and larger NQ particle sizes. The rings within the patterns were separated by greater distances and the patterns themselves varied quite a bit from region to region. To explain why this is so may be a topic for future investigations, but this difference indicates that control over the morphology may be possible.

The lack of ring structure formation in the lots that were remixed is strong evidence that the pin plate feed holes are a critical element in the resulting morphology. Figure 14, as in Figure 6, shows the various stages propellant encounters during the extrusion process, and illustrates the pin plate and feed hole orientation used for the propellant grains and strands examined in this study. The following is offered as a possible mechanism for the ring structure formation. The propellant billet, with an NQ crystal

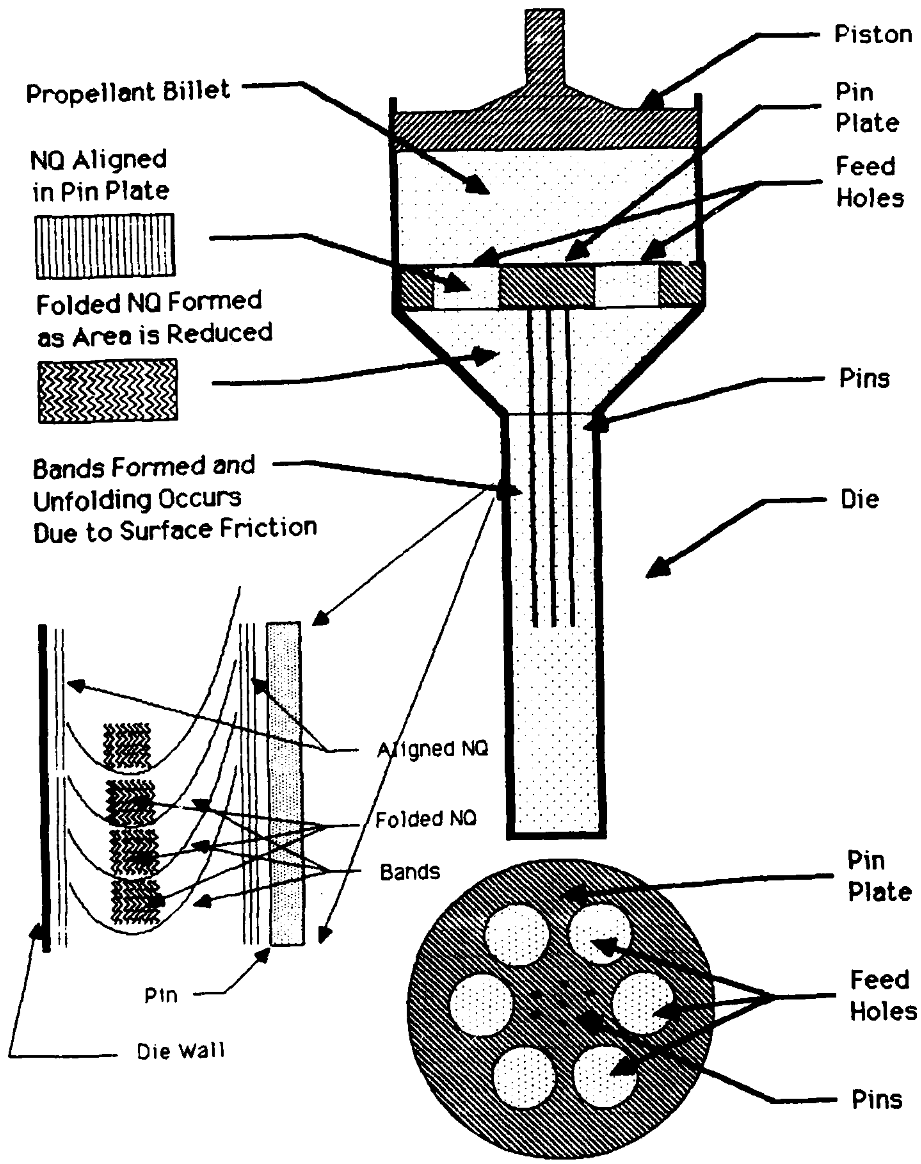

Figure 14. Schematic Diagram Illustrating the Extrusion Process and a Possible Method for the Formation of Bands of Folded NQ within the Grain

orientation determined by mixing and assumed to be random or in randomly oriented "domains" (similar to ferromagnetic domains in a nonmagnetic piece of iron), is loaded into the press. The piston forces the putty-like material through the six feed holes in the pin plate causing the long NQ crystals to be oriented in the direction of flow due to differential flow across the feed hole. As the material is forced into the section with decreasing cross-sectional area, the constriction causes NQ folding in each of the six "columns" under the holes. The greater the constriction during this part of the process results in tighter folding of the NQ. The propellant then enters the region containing the perforation pins. The propellant containing folded NQ that is near any surface becomes unfolded due to the velocity gradient

caused by surface friction. In areas farther removed from the surfaces the propellant flows more freely, leaving this portion folded and moving more quickly. The result is a curved band of folded material that gradually becomes completely aligned with the direction of extrusion near the die or pin surface - the condition discovered in all of the propellant lots.

In the case of the solid strands, the pinplate acted in a similar fashion, except the removal of the pins permitted the ring pattern to spread because no pin surface friction was available to align the NQ in the interior of the die. NQ alignment in the center of the strand, which was strong but not as strong as that near an extrusion surface, could be the result of differential, viscous flow. The center of each ring structure corresponds to the region of highest mass flow during extrusion. Surface friction or flow restriction, due to lower pressure regions created in "dead spaces" under the pin plate and away from the feed holes, cause gradual alignment of the NQ away from the ring centers. The remixed strands extruded without the pinplate have the NQ aligned by the velocity gradient across the entire strand diameter. The observed gentle folding at the center of the strand reflects the relative ease with which the propellant was extruded, and may indicate that the entire die is acting as a single large feed hole. Thus, the pin plate seems to be the key element responsible for the formation and structure of the observed ring patterns.

B. Effects of Propellant Morphology

The propellant mechanical properties do not seem significantly affected by the morphological differences between the lots. As reported above, the modulus values were very similar. In addition, transitions indicated by tan delta (the ratio of the loss to the tensile modulus) which can be used to gage fracture response are also very similar. Figure 15 shows the modulus and tan delta plotted as a function of temperature for the normal NQ strand extruded with the pin plate in position. The low temperature transition, indicating embrittlement, and the onset of the high temperature transition, occur at these same temperatures in each of the lots. If the fracture response of two lots were significantly different, the tan delta curve would be expected to show a difference as well. So it seems that the mechanical response is not strongly affected by the change in morphology. Therefore, no significant performance differences due to mechanical response differences are indicated.

Another possible mechanism which could affect the gun performance is a change of burning characteristics with morphology. For example, it is well known that porosity in propellant causes a more rapid mass generation than in a lower porosity propellant of the same formulation. This is due to the increased area provided to the flame front and, perhaps, to an increase in the propellant grain fracture susceptibility. So it is not unreasonable to suspect that a change in morphology might cause a change in the burning rate.

During ignition of propellant that contains the NQ morphology observed here, the flame is initiated on the same outside surface that helped to cause the alignment of NQ crystals. The NQ structure exposed to the flame, therefore, changes as the grain burns, and an effect similar to a change in porosity may take place. Initially the flame front proceeds in a direction

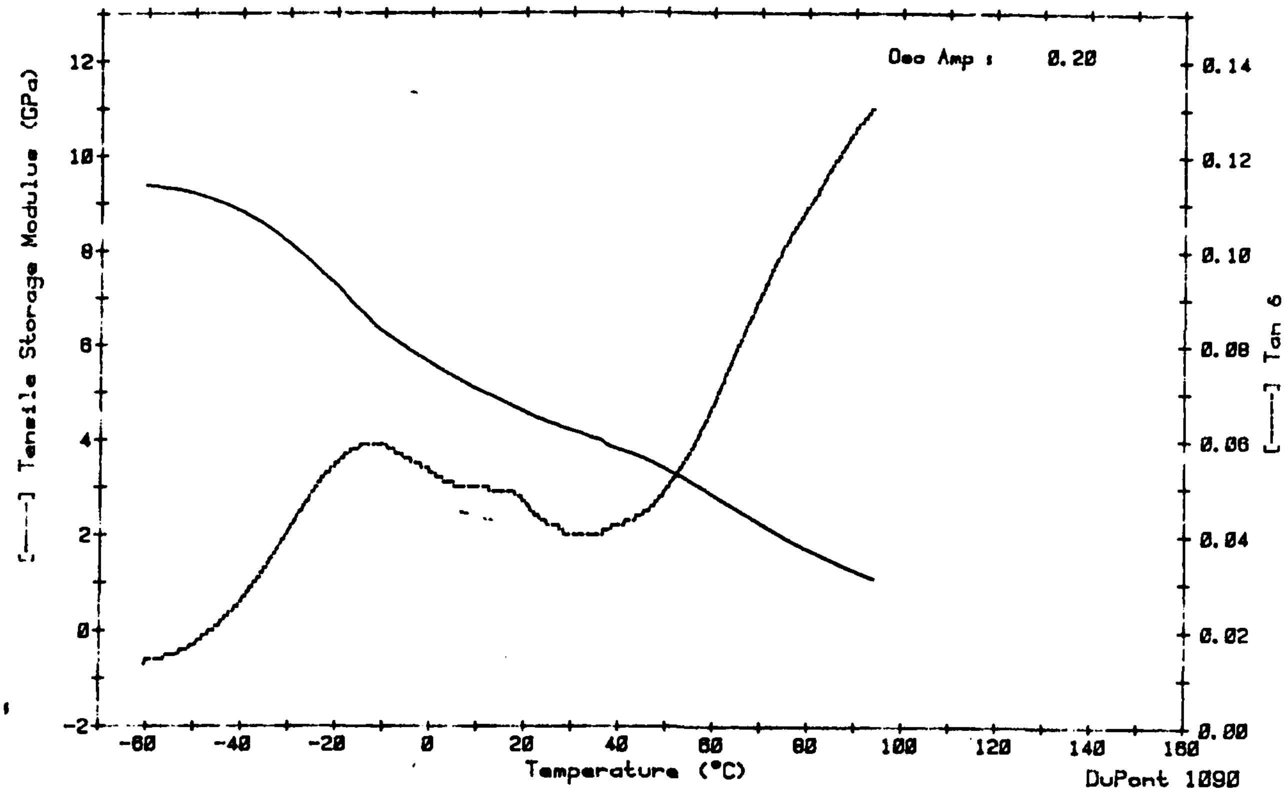

Figure 15. Representative Dynamic Mechanical Analysis Results
Showing Modulus and Tan Delta vs Temperature for M30

perpendicular to the NQ alignment on all surfaces except the grain ends. As burning progresses, the regions in which there is NQ folding become exposed. If the ends of NQ crystals have different ignitability, or intrinsic burning rate than sides of the crystals, the rate of mass generation may change. While there is no direct evidence for this conjecture, burning rate curves calculated from M30 closed bomb pressure-time data show breaks that indicate a change in burning character.

Figure 16 shows one of six burning rate vs pressure plots examined for M30 Lot 67878, which showed ring structure. The break in this and all the other curves occurs at about 10 kpsi. The average distance burned, calculated

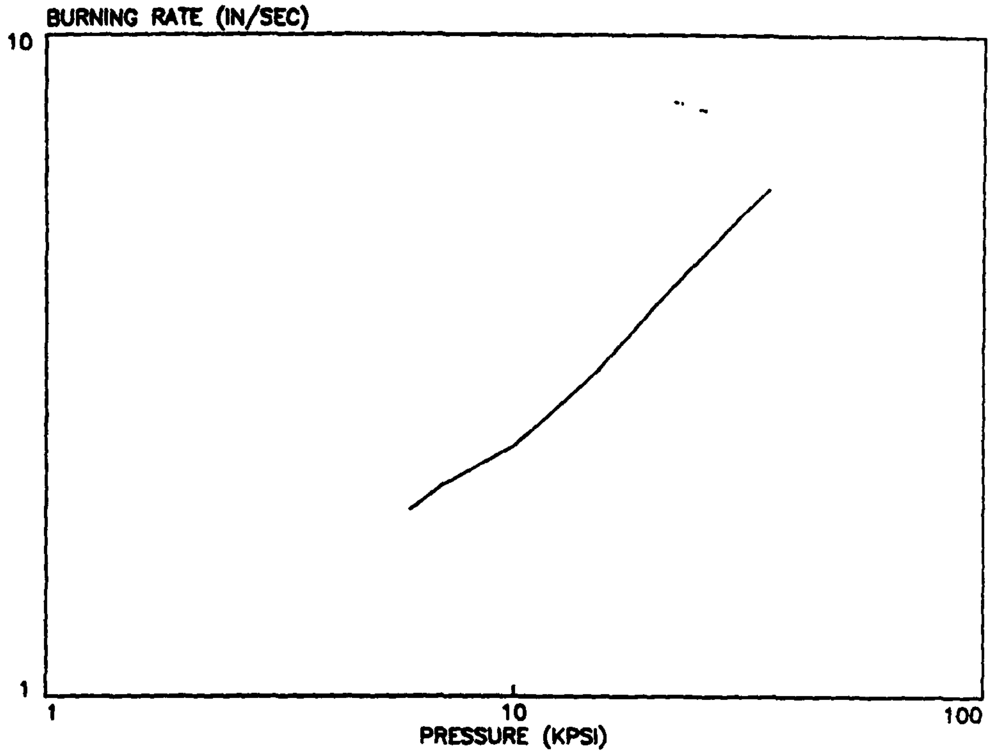

Figure 16. Closed Bomb Burning Rate vs Pressure for M30 Showing a Slope Break at about 10 kpsi (69 MPa)

from the closed bomb data analysis program CBRED2[6], corresponding to this pressure is 0.171 mm. The average distance from the perforation surface to the first ring in this lot of M30, which should be a measure of when folded NQ crystals are becoming exposed to the flame front, is 0.185 mm. The closeness of these two distances suggest the possibility of a causal relationship between the onset of the morphology change and the slope break.

As a follow-up study, a series of closed bomb experiments was performed to investigate the relationship suggested above. In closed bomb testing, a measured mass of the propellant to be investigated is placed into the known volume of the bomb. This mass to volume ratio is called the loading density. The propellant is uniformly ignited and the pressure-time data is recorded for the fixed bomb volume. Since the pressure at any time depends on the amount of gas generated, its temperature, the heat loss of the bomb, and a host of

---

[6]C. Price and A. Juhasz, "A Versatile User-Oriented Closed Bomb Data Reduction Program (CBRED)," BRL Report 2018, USA ARRADCOM, Ballistic Research Laboratory, Aberdeen Proving Ground, Maryland, September 1977.

other known thermodynamic parameters, the rate of gas generation can be determined. From this the burning rate of the propellant is easily determined since the total surface area can be calculated from grain geometry. This finally allows the Burning Rate vs Pressure to be plotted.

These closed bomb burning rates were measured for M30 Lot 67878 at loading densities of 0.20, 0.25, 0.30, and 0.35 g/cc. Three firings were made at each loading density. If a change in NQ morphology causes a change in the rate of mass generation, as the loading density is increased, the slope break in the Burning Rate vs Pressure Curve should occur at increased pressure. This is due to the greater mass generation occurring before the change in morphology is encountered at the higher loading density firings. However, if the break is a result of chemical changes dependent on pressure and independent of the morphology, the break should occur at the same pressure regardless of loading density. The results, shown in Figure 17, show that the pressure at the break in slope increases almost linearly as the loading density is increased. In addition, the distance burned at the pressure corresponding to the slope break, listed in Table 2, is nearly constant at every loading density. The average value of the distance burned at slope break is 0.213 mm. A direct comparison of this value and the distance to ring onset (0.185 mm) is not particularly meaningful since the distance burned values can shift appreciably depending on initial values chosen in the reduction program (CBRED2). What is significant is that the physically measured distance and the calculated distance burned values are reasonably close, that the slope break increases with increasing loading density, and that using the same reduction program variables the distance burned was nearly constant at each slope break. It seems as if the burning rate is affected by the NQ morphology. This implies that a measure of control can be had on the burning rate of NQ based propellants by controlling the NQ morphology within the grain.

TABLE 2. DISTANCE BURNED AT SLOPE BREAK

Pressure at Slope Break	Distance Burned	Loading Density
55.2 MPa	0.222 mm	0.200 g/cc
71.1	0.212	0.254
84.9	0.211	0.297
97.3	0.208	0.344

IV. CONCLUSIONS

The ring structure observed for the M31A1 and M30 propellants studied here has been explained by the discovery of underlying bands of folded NQ within the propellant. Strong evidence suggests that the pin plate feed holes control the formation of these structures during extrusion. Perforation pins

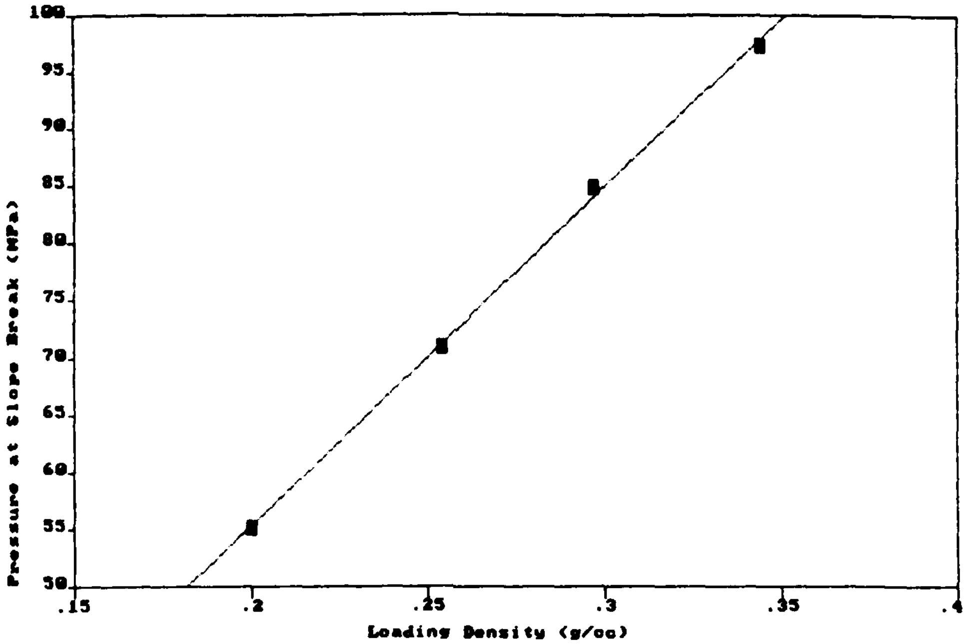

Figure 17. Pressure at Slope Break vs Loading Density
from Closed Bomb Burning Rate Studies

cause surface friction which locally aligns the NQ crystals and alters the shape of the ring structure, but the pins are not essential to the band or the NQ folding formation. The ring structure is also affected by the propellant physical dimensions and by NQ particle size. Smaller webs and smaller particle sizes produce more well defined and higher density ring structures. Propellant extruded without the pin plate in place showed no band or ring structure. NQ alignment in these samples was in the direction of extrusion due to viscous flow and only a slight crystal folding resulting from reduced resistance to flow was observed. Since pin plates are required for the production of perforated grains, the ring structure should be a common feature in NQ-based propellants.

There is no indication that the mechanical response of the propellant is affected by the morphological differences observed here. Both the mechanical properties and the phase transitions measured using dynamic mechanical analysis produced almost identical results for propellant strands with and without the ring structure. The length of the NQ crystals also produced no mechanical response differences.

Closed bomb results and analysis show that the break in the burning rate curve observed for M30 corresponds to the flame front encountering a changing morphological structure. As predicted, the pressure at which the slope break occurs, from the Burning Rate vs Pressure Curve, increases as propellant

loading density increases. In addition, the propellant distance burned at the slope break point remains constant at all loading densities and compares fairly well with the physical distance between the outer perforation surface and the first observed ring. This implies that the burning rate of NQ based propellants can be controlled to some degree if the NQ morphology within the grain can be controlled.

For a more complete understanding of the role that this newly discovered NQ morphology plays in propellant combustion, several research areas need to be continued. The NQ orientation should be determined at each stage of the extrusion process so that factors controlling the NQ morphology may be understood and exploited. Low pressure strand burning rates should be established using propellant strands with known, orthogonal NQ orientation to establish burning rate differences at known orientations. Propellants with pin plate feed hole patterns with other symmetries should be examined to determine the effect of different feed hole design of the resulting morphology.

If these processes can be understood and controlled, improvements in the mechanical properties and burning characteristics may be possible. This would lead to safer, less vulnerable propellants with better performance.

V. ACKNOWLEDGMENT

The authors would like to express thanks to Dr. Arpad A. Juhasz from the Advanced Ballistic Concepts Branch of the Ballistic Research Laboratory for his valuable input during discussions of closed bomb testing of gun propellant.

REFERENCES

1. C. W. Fong and B. K. Moy, "Ballistic Criteria for Propellant Grain Fracture In the GAU-8/A 30MM Gun," Technical Report AFATL-TR-82-21, Air Force Armament Laboratory, Direct Fire Weapons Division, Eglin AFB, Florida, March 1982.

2. P. Benhaim, J. L. Paulin, B. Zeller, "Investigation on Gun Propellant Break-Up and Its Effect in Interior Ballistics," Proceedings of the 4th International Symposium on Ballistics, Monterey, CA, October 1978.

3. A. W. Horst, I. W. May, and E. V. Clark "The Missing Link Between Pressure Waves and Breechblows," Ballistic Research Laboratory Report ARBRL-MR-02849, July 1978.

4. R. L. Hassel, "Evaluating Polymers by Dynamic Mechanical Analysis," Plastics Engineering, Vol. 33, No. 10, October 1977.

5. R. J. Lieb, and J. J. Rocchio, "Standardization of a Drop Weight Mechanical Properties Tester for Gun Propellants," Technical Report ARBRL-TR-02516, USA ARRADCOM Ballistic Research Laboratory, Aberdeen Proving Ground, Maryland, July 1983.

6. C. Price and A. Juhasz, "A Versatile User-Oriented Closed Bomb Data Reduction Program (CBRED)," BRL Report 2018, USA ARRADCOM, Ballistic Research Laboratory, Aberdeen Proving Ground, Maryland, September 1977.

This page is left intentionally blank.

DISTRIBUTION LIST

No. Of Copies	Organization	No. Of Copies	Organization
12	Administrator Defense Technical Info Center ATTN: DTIC-DDA Cameron Station Alexandria, VA 22304-6145	1	Commander US Army Materiel Command ATTN: AMCDRA-ST 5001 Eisenhower Avenue Alexandria, VA 22333-5001
1	Commander USA Concepts Analysis Agency ATTN: D. Hardison 8120 Woodmont Avenue Bethesda, MD 20014-2797	1	Commander US Army Materiel Command ATTN: AMCDE-DW 5001 Eisenhower Avenue Alexandria, VA 22333-5001
1	HQDA/DAMA-ZA Washington, DC 20310-2500	5	Project Manager Cannon Artillery Weapons System, ARDEC, AMCCOM ATTN: AMCPM-CW, F. Menke AMCPM-CWW AMCPM-CWS M. Fisette AMCPM-CWA R. DeKleine H. Hassmann Dover, NJ 07801-5001
1	HQDA, SARDA Washington, DC 20310-2500	2	Project Manager Munitions Production Base Modernization and Expansion ATTN: AMCPM-PBM, A. Siklosi AMCPM-PBM-E, L. Laibson Dover, NJ 07801-5001
1	Commander US Army War College ATTN: Library-FF229 Carlisle Barracks, PA 17013	3	Project Manager Tank Main Armament Systems ATTN: AMCPM-TMA, K. Russell AMCPM-TMA-105 AMCPM-TMA-120 Dover, NJ 07801-5001
1	US Army Ballistic Missile Defense Systems Command Advanced Technology Center P.O. Box 1500 Huntsville, AL 35807-3801	1	Commander US Army Watervliet Arsenal ATTN: SARWV-RD, R. Thierry Watervliet, NY 12189-5001

No. Of Copies	Organization
1	Chairman DOD Explosives Safety Board Room 856-C Hoffman Bldg. 1 2461 Eisenhower Avenue Alexandria, VA 22331-9999
1	Commander US Army Material Command ATTN: AMCPM-GCM-WF 5001 Eisenhower Avenue Alexandria, VA 22333-5001
1	Commander Armament R&D Center US Army AMCCOM ATTN: SMCAR-TDC Dover, NJ 07801
4	Commander US Army Armament Munitions and Chemical Command ATTN: SMCAR-ESP-L Rock Island, IL 61299-7300
1	Commander US Army Aviation Research and Development Command ATTN: AMSAV-E 4300 Goodfellow Blvd. St. Louis, MO 63120-1702

No. Of Copies	Organization
1	Commander Armament R&D Center US Army AMCCOM ATTN: SMCAR-TSS Dover, NJ 07801-5001
20	Commander US Army ARDC, AMCCOM ATTN: SMCAR-TSS SMCAR-TDC SMCAR-LC LTC N. Baron SMCAR-LCA A. Beardell D. Downs S. Einstein S. Westley S. Bernstein C. Roller J. Rutkowski SMCAR-LCB-I D. Spring SMCAR-LCE SMCAR-LCM-E S. Kaplowitz SMCAR-LCS SMCAR-LCU-CT E. Barrieres R. Davitt SMCAR-LCU-CV C. Mandala SMCAR-LCW-A M. Salsbury SMCAR-SCA L. Stiefel B. Brodman Dover, NJ 07801-5001
1	Director Benet Weapons Laboratory Armament R&D Center US Army AMCCOM ATTN: SMCAR-LCB-TL Watervliet, NY 12189-5001
1	Commander US Army TSARCOM 4300 Goodfellow Blvd. St. Louis, MO 63120-1702

No. Of Copies	Organization	No. Of Copies	Organization
1	HQDA DAMA-ART-M Washington, DC 20310-2500	1	Commander US Army Communications Electronics Command ATTN: AMSEL-ED Fort Monmouth, NJ 07703-5301
1	Director US Army Air Mobility Research and Development Laboratory Ames Research Center Moffett Field, CA 94035-1099	1	Commander ERADCOM Technical Library ATTN: DELSD-L (Report Section) Fort Monmouth, NJ 07703-5301
1	Commander US Army Harry Diamond Lab ATTN: DELHD-TA-L 2800 Powder Mill Road Adelphi, MD 20783-1145	1	Commander US Army Missile Command ATTN: AMSMI-CM Redstone Arsenal, AL 35898-5249
1	Commander US Army Missile and Space Intelligence Center ATTN: AIAMS-YDL Redstone Arsenal, AL 35898-5500	1	President US Army Armor & Engineer Board ATTN: ATZK-AD-S Fort Knox, KY 40121-5200
1	Commander US Army Missle Command Research, Development, and Engineering Center ATTN: AMSMI-RD Redstone Arsenal, AL 35898-5500	1	Project Manager M-60 Tank Development ATTN: AMCPM-M60TD Warren, MI 48092-2498
1	Commandant US Army Aviation School ATTN: Aviation Agency Fort Rucker, AL 36360	1	Director US Army TRADOC Systems Analysis Activity ATTN: ATAA-SL White Sands Missle Range, NM 88002
1	Commander US Army Tank Automotive Command ATTN: AMSTA-TSL Warren, MI 48397-5000	1	Commander US Army Training & Doctrine Command ATTN: ATCD-MA/Maj Williams Fort Monroe, VA 23651
1	Commander US Army Tank Automotive Command ATTN: AMSTA-CG Warren, MI 48397-5000	2	Commander US Army Materials and Mechanics Research Center ATTN: AMXMR-ATL Tech Library Watertown, MA 02172

No. Of Copies	Organization	No. Of Copies	Organization
1	Project Manager Improved TOW Vehicle ATTN: AMCPM-ITV US Army Tank Automotive Command Warren, MI 48397-5000	1	Commander US Army Research Office ATTN: Tech Library P.O. Box 12211 Research Triangle Park, NC 27709-2211
2	Program Manager M1 Abrams Tank System ATTN: AMCPM-GMC-SA, T. Dean Warren, MI 48092-2498	1	Commander US Army Belvoir Research & Development Center ATTN: STRBE-WC Fort Belvoir, VA 22060-5606
1	Project Manager Fighting Vehicle Systems ATTN: AMCPM-FVS Warren, MI 48092-2498	1	Commander US Army Logistics Mgmt Ctr Defense Logistics Studies Fort Lee, VA 23801
1	Commandant US Army Infantry School ATTN: ATSH-CD-CSO-OR Fort Benning, GA 31905		
1	Office of Naval Research ATTN: Code 473, R.S. Miller 800 N. Quincy Street Arlington, VA 22217-9999	1	President US Army Artillery Board Ft. Sill, OK 73503-5600
1	Commandant US Army Command and General Staff College Fort Leavenworth, KS 66027	3	Commandant US Army Armor School ATTN: ATZK-CD-MS M. Falkovitch Armor Agency Fort Knox, KY 40121-5215
1	Commandant US Army Special Warfare School ATTN: Rev & Tng Lit Div Fort Bragg, NC 28307	2	Commander Naval Sea Systems Command ATTN: SEA 62R SEA 64 Washington, DC 20362-5101
3	Commander Radford Army Ammunition Plant ATTN: SMCRA-QA/HI LIB Radford, VA 24141-0298	1	Commander Naval Air Systems Command ATTN: AIR-954-Tech Lib Washington, DC 20360
1	Commander US Army Foreign Science & Technology Center ATTN: AMXST-MC-3 220 Seventh Street, NE Charlottesville, VA 22901-5396	1	Assistant Secretary of the Navy (R, E, and S) ATTN: R. Reichenbach Room 5E787 Pentagon Bldg. Washington, DC 20350

1 Naval Research Lab
Tech Library
Washington, DC 20375

5 Commander
Naval Surface Weapons Center
ATTN: Code G33, J.L. East
W. Burrell
J. Johndrow
Code G23, D. McClure
Code DX-21 Tech Lib
Dahlgren, VA 22448-5000

2 Commander
US Naval Surface Weapons Center
ATTN: J.P. Consaga
C. Gotzmer
Indian Head, MD 20640-5000

4 Commander
Naval Surface Weapons Center
ATTN: S. Jacobs/Code 240
Code 730
K. Kim/Code R-13
R. Bernecker
Silver Springs, MD 20903-5000

2 Commanding Officer
Naval Underwater Systems Center
Energy Conversion Dept.
ATTN: Code 5B331, R.S. Lazar
Tech Library
Newpoprt, RI 02840

4 Commander
Naval Weapons Center
ATTN: Code 388, R.L. Derr
C.F. Price
T. Boggs
Info. Sci. Div.
China Lake, CA 93555-6001

2 Superintendent
Naval Postgraduate School
Department of Mechanical Engineering
Monterey, CA 93943-5100

2 Commandant
US Army Field Artillery Center & School
ATTN: ATSF-CO-MW, B. Willis
Ft. Sill, OK 73503-5600

1 Commander
US Army Development and Employment Agency
ATTN: MODE-TED-SAB
Fort Lewis, WA 98433-5099

6 Commander
Naval Ordnance Station
ATTN: P.L. Stang
J. Birkett
L. Torreyson
T.C. Smith
D. Brooks
Tech Library
Indian Head, MD 20640-5000

1 AFSC/SDOA
Andrews AFB, MD 20334

1 AFRPL/DY, Stop 24
ATTN: J. Levine/DYCR
R. Corley/DYC
D. Williams/DYCC
Edwards AFB, CA 93523-5000

1 AFRPL/TSTL (Tech Library)
Stop 24
Edwards AFB, CA 93523-5000

1 AFATL/DLYV
Eglin AFB, FL 32542-5000

1 AFATL/DLXP
Eglin AFB, FL 32542-5000

1 AFATL/DLJE
Eglin AFB, FL 32542-5000

1 AFATL/DLODL
ATTN: Tech Library
Eglin AFB, FL 32542-5000

1	AFWL/SUL Kirtland AFB, NM 87117	1	Program Manager AFOSR Directorate of Aerospace Sciences ATTN: L.H. Caveny Bolling AFB, DC 20332-0001
1	NASA/Lyndon B. Johnson Space Center ATTN: NHS-22, Library Section Houston, TX 77054	2	Calspan Corporation ATTN: C. Morphy P.O. Box 400 Buffalo, NY 14225-0400
1	AFELM, The Rand Corporation ATTN: Library D (Required or Classified only) 1700 Main Street Santa Monica, CA 90401-3297	10	Central Intelligence Agency Office of Central Reference Dissemination Branch Room GE-47 HQS Washington, DC 20505
1	General Applied Sciences Lab ATTN: J. Erdos Merrick & Stewart Avenues Westbury Long Island, NY 11590	1	General Electric Company Armament Systems Dept. ATTN: M.J. Bulman, Room 1311 128 Lakeside Avenue Burlington, VT 05401-4985
1	AAI Corporation ATTN: J. Hebert J. Frankle P.O. Box 6767 Baltimore, MD 21204	1	IITRI ATTN: M.J. Klein 10 W. 35th Street Chicago, IL 60616-3799
		1	Hercules, Inc. Allegheny Ballistics Laboratory ATTN: R.B. Miller P.O. Box 210 Cumberland, MD 21501-0210
1	Aerojet Ordnance Company ATTN: D. Thatcher 2521 Michelle Drive Tustin, CA 92680-7014	1	Hercules, Inc. Bacchus Works ATTN: K.P. McCarty P.O. Box 98 Magna, UT 84044-0098
1	Aerojet Solid Propulsion Co. ATTN: P. Micheli Sacramento, CA 95813	1	Hercules, Inc. Radford Army Ammunition Plant ATTN: J. Pierce Radford, VA 24141-0299
1	Atlantic Research Corporation ATTN: M.K. King 5390 Cheorokee Avenue Alexandria, VA 22312-2302	1	AVCO Everett Rsch Lab ATTN: D. Stickler 2385 Revere Beach Parkway Everett, MA 02149-5936

No. Of Copies	Organization	No. Of Copies	Organization
1	Honeywell, Inc - MN64 2200 Defense Systems Division ATTN: C. Hargreaves 6110 Blue Circle Drive Minnetonka, MN 55436	1	Princeton Combustion Research Lab., Inc. ATTN: M. Summerfield 475 US Highway One Monmouth Junction, NJ 08852-9650
1	Lawrence Livermore National Laboratory ATTN: L-355, A. Buckingham M. Finger P.O. Box 808 Livermore, CA 94550-0622	2	Rockwell International Rocketdyne Division ATTN: BA08 J.E. Flanagan J. Gray 6633 Canoga Avenue Canoga Park, CA 91303-2703
1	Lawrence Livermore National Laboratory ATTN: L-324 M. Constantino P.O. Box 808 Livermore, CA 94550-0622	1	Science Applications, Inc. ATTN: R.B. Edelman 23146 Cumorah Crest Drive Woodland Hills, CA 91364-3710
		3	Thiokol Corporation Huntsville Division ATTN: D. FLanigan R. Glick Tech Library Huntsville, AL 35807
1	Olin Corporation Badger Army Ammunition Plant ATTN: R.J. Thiede Baraboo, WI 53913		
1	Olin Corporation Smokeless Powder Operations ATTN: D.C. Mann P.O. Box 222 St. Marks, FL 32355-0222	1	Scientific Research Assoc., Inc. ATTN: H. McDonald P.O. Box 498 Glastonbury, CT 06033-0498
1	Paul Gough Associates, Inc. ATTN: P.S. Gough P.O. Box 1614, 1048 South St. Portsmouth, NH 03801-1614	1	Veritay Technology, Inc. ATTN: E. Fisher 4845 Millersport Hwy. P.O. Box 305 East Amherst, NY 14051-0305
1	Physics International Company ATTN: Library H. Wayne Wampler 2700 Merced Street San Leandro, CA 94577-5602	2	Thiokol Corporation Elkton Division ATTN: R. Biddle Tech Lib. P.O. Box 241 Elkton, MD 21921-0241
2	United Technologies Chemical Systems Division ATTN: R. Brown Tech Library P.O. Box 358 Sunnyvale, CA 94086-9998	1	University of Massachusetts Dept. of Mechanical Engineering ATTN: K. Jakus Amherst, MA 01002-0014

No. Of Copies	Organization	No. Of Copies	Organization
		1	University of Minnesota Dept of Mechanical Engineering ATTN: E. Fletcher Minneapolis, MN 55414-3368
1	Universal Propulsion Company ATTN: H.J. McSpadden Black Canyon Stage 1 Box 1140 Phoenix, AZ 85029	1	Case Western Reserve University Division of Aerospace Sciences ATTN: J. Tien Cleveland, OH 44135
1	Battelle Memorial Institute ATTN: Tech Library 505 King Avenue Columbus, OH 43201-2693	3	Georgia Institute of Tech School of Aerospace Eng. ATTN: B.T. Zinn E. Price W.C. Strahle Atlanta, GA 30332
1	Brigham Young University Dept of Chemical Engineering ATTN: M. Beckstead Provo, UT 84601	1	Institute of Gas Technology ATTN: D. Gidaspow 3424 S. State Street Chicago, IL 60616-3896
1	California Institute of Tech 204 Karman Lab Main Stop 301-46 ATTN: F.E.C. Culick 1201 E. California Street Pasadena, CA 91109	1	Johns Hopkins University Applied Physics Laboratory Chemical Propulsion Information Agency ATTN: T. Christian Johns Hopkins Road Laurel, MD 20707-0690
1	California Institute of Tech Jet Propulsion Laboratory ATTN: L.D. Strand 4800 Oak Grove Drive Pasadena, CA 91109-8099	1	Massachusetts Institute of Technology Dept of Mechanical Engineering ATTN: T. Toong 77 Massachusetts Ave Cambridge, MA 02139-4307
1	University of Illinois Dept of Mech/Indust Engr ATTN: H. Krier 144 MEB; 1206 N. Green St. Urbana, IL 61801-2978	1	G.M. Faeth Pennsylvania State University Applied Research Laboratory University Park, PA 16802-7501

No. Of Copies	Organization	No. Of Copies	Organization
1	University of Southern California Mechanical Engineering Dept. ATTN: OHE200, M. Gerstein Los Angeles, CA 90089-5199	1	Pennsylvania State University Dept of Mech. Engineering ATTN: K. Kuo University Park, PA 16802-7501
2	University of Utah Dept of Chemical Engineering ATTN: A. Baer G. Flandro Salt Lake City, UT 84112-1194	1	Purdue University School of Mechanical Engineering ATTN: J.R. Osborn TSPC Chaffee Hall West Lafayette, IN 47907-1199
1	Washington State University Dept of Mechanical Engineering ATTN: C.T. Crowe Pullman, WA 99163-5201	1	SRI International Propulsion Sciences Division ATTN: Tech Library 333 Ravenswood Ave Menlo Park, CA 94025-3493
1	Rensselaer Polytechnica Inst. Department of Mathematics Troy, NY 12181	1	Stevens Institute of Technology Davidson Laboratory ATTN: R. McAlevy, III Castle Point Station Hoboken, NJ 07030-5907
1	Rutgers University Dept of Mechanical and Aerospace Engineering ATTN: S. Temkin University Heights Campus New Brunswick, NJ 08903		

Aberdeen Proving Ground

Dir, USAMSAA
ATTN: AMXSY-D
AMXSY-MP, H. Cohen
Cdr, USATECOM
ATTN: AMSTE-TO-F
AMSTE-CM-F, L. Nealley
Cdr, CSTA
ATTN: STECS-AS-H, R. Hendricksen
Cdr, CRDEC, AMCCOM
ATTN: SMCCR-RSP-A
SMCCR-MU
SMCCR-SPS-IL